Letter

Probing quantum geometric nonlinear magnetization via second-harmonic magneto-optical Kerr effect

Xuan Qian,[1,2,*] Xiao-Bin Qiang,[3,*] Wenkai Zhu,[1,2,*] Yuqing Huang,[1,2] Yiyuan Chen,[3,4] Hai-Zhou Lu,[3,4,†]
Yang Ji,[5,‡] and Kaiyou Wang[1,2,§]
[1]*State Key Laboratory of Semiconductor Physics and Chip Technologies, Institute of Semiconductors, Chinese Academy of Sciences, Beijing 100083, China*
[2]*College of Materials Science and Optic-Electronic Technology, University of Chinese Academy of Sciences, Beijing 100049, China*
[3]*State Key Laboratory of Quantum Functional Materials, Department of Physics, and Guangdong Basic Research Center of Excellence for Quantum Science, Southern University of Science and Technology (SUSTech), Shenzhen 518055, China*
[4]*Quantum Science Center of Guangdong-Hong Kong-Macao Greater Bay Area (Guangdong), Shenzhen 518045, China*
[5]*School of Physics, Zhejiang University, Hangzhou, China*

(Received 7 July 2025; revised 4 January 2026; accepted 9 January 2026; published 29 January 2026)

Quantum geometry provides an intrinsic framework for characterizing the geometric structure of quantum states. It highlights its relevance to various aspects of fundamental physics. However, its direct implications for magnetic phenomena remain largely unexplored. Here, we report the observation of electric-field-induced nonlinear magnetization in the nonmagnetic semimetal WTe_2 by using a second-harmonic magneto-optical Kerr effect (SMOKE) spectroscopy. We observe a robust nonlinear SMOKE signal that scales quadratically with current and persists up to 200 K. Theoretical modeling and scaling analysis indicate that this nonlinear magnetization is dominated by the orbital contribution and is intrinsically linked to the quantum Christoffel symbol. Just as the Christoffel symbol is a fundamental quantity encoding spacetime geometry in Einstein's general relativity, our work establishes a direct link between quantum geometry and nonlinear magnetization, and provides a geometric perspective for designing future orbitronic devices.

DOI: 10.1103/dww3-vm74

Introduction. Quantum geometry ($\mathbf{g} - i\mathbf{\Omega}/2$) characterizes the distance between quantum states in parameter space [1–3]. Its imaginary part corresponds to the Berry curvature $\mathbf{\Omega}$, which quantifies the phase distance, while its real part defines the quantum metric $\mathbf{g}$, quantifying the amplitude distance. Recent studies have highlighted its pivotal role in a range of phenomena [4–6], including flat-band superconductors [7–11], fractional Chern insulators [12–14], and nonlinear transport [15–24]. In the area of magnetic responses [25–38], the Berry curvature provides a well-established description of linear magnetization ($\mathbf{M} \propto \mathbf{E}$, where $\mathbf{M}$ is the magnetization and $\mathbf{E}$ is the electric field) [39–50]. Nevertheless, the influence of the quantum metric $\mathbf{g}$ on magnetic responses, especially in the nonlinear regime ($\mathbf{M} \propto \mathbf{EE}$), remains largely unexplored. This gap stems from the difficulty of detecting weak magnetic signals and the lack of a systematic theory for higher-order effects.

In this Letter, we report the observation of electric-field-induced nonlinear magnetization in the nonmagnetic semimetal WTe_2. This was achieved by developing a high-sensitivity SMOKE spectroscopy that employs lock-in detection to isolate the second-harmonic Kerr signals from background noise [Figs. 1(a) and 1(b)]. Therefore, this technique extends conventional magneto-optical Kerr effect (MOKE) [51–56] into the nonlinear regime. We observed a robust SMOKE signal that scales quadratically with the applied electric field up to 200 K. Symmetry analysis and theoretical calculations further reveal that this nonlinear magnetization is dominated by orbital contribution, which can be heuristically understood through the field-induced deformation of Bloch wavepackets [Fig. 1(c)]. Strikingly, this deformation is fundamentally governed by a geometric quantity, the quantum Christoffel symbol, which is directly related to the quantum metric $\mathbf{g}$ [Eq. (4)]. The additional scaling analysis shows that the experimental data are in good agreement with theoretical predictions across a broad range of temperatures.

Demonstration of mirror symmetry breaking. According to the symmetry analysis presented in Sec. SI in the Supplemental Material [57], an out-of-plane nonlinear magnetization M_c induced by an in-plane electric field E_a requires breaking both the twofold rotational symmetries ($\mathcal{C}_a^2$ and $\mathcal{C}_b^2$) and the mirror symmetries ($\mathcal{M}_a$ and $\mathcal{M}_b$), where (a, b, c) represent crystallographic directions. This requirement suggests that multilayer Td-phase WTe_2, a nonmagnetic semimetal, could serve as a promising candidate. As shown in Fig. 2(a), ideal multilayer WTe_2 preserves only a single mirror symmetry $\mathcal{M}_a$. However, in realistic devices, this residual symmetry is typically weakly broken due to interface and strain effects [58–61]. To determine whether $\mathcal{M}_a$ is similarly broken in our

---

[*] These authors contributed equally to this work.
[†] Contact author: luhz@sustech.edu.cn
[‡] Contact author: jiyang2024@zju.edu.cn
[§] Contact author: kywang@semi.ac.cn

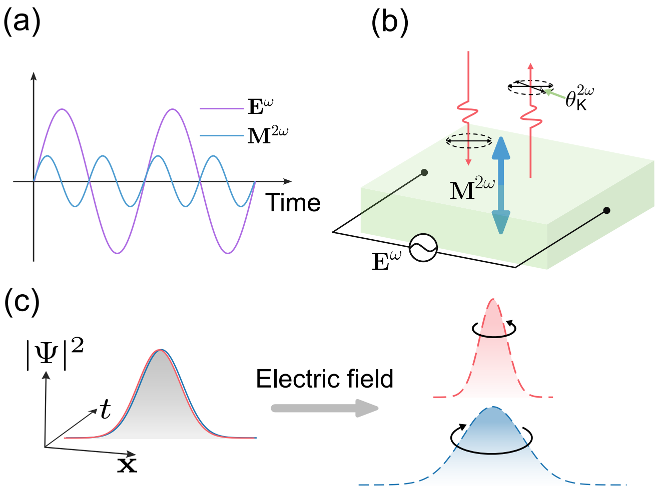

FIG. 1. SMOKE detection and quantum geometric nonlinear magnetization. (a) Demonstration of second-harmonic nonlinear magnetization $\mathbf{M}^{2\omega}$ at frequency 2ω induced by an alternating electric field $\mathbf{E}^{\omega}$ at frequency ω, i.e., ($\mathbf{M}^{2\omega} \propto \mathbf{E}^{\omega}\mathbf{E}^{\omega}$). (b) Schematic of SMOKE detection to the nonlinear magnetization, the red downward (upward) arrow represents incident (reflected) light, the green arrow represents induced magnetization with frequency 2ω, and the purple arrow represents applied alternating electric field with frequency ω. (c) Schematic of nonlinear magnetization origin. Orbital magnetization arises from the self-rotation of Bloch wavepacket (circular arrows) [15,39]. An applied electric field modifies the wave packets (solid to dashed curves) and induces a nonequilibrium distribution. This prevents the mutual cancellation of time-reversal counterparts (red and blue), and leads to a quadratic electric-field dependence.

devices, we utilize the nonlinear Hall effect as a probe. Since $\mathcal{M}_a$ also forbids the nonlinear Hall response when the current is applied along the *b* axis [16–18], the observation of such a signal can provide direct evidence of $\mathcal{M}_a$ breaking.

For the nonlinear Hall measurements, we utilized a device incorporating a ∼7 nm thick Td-phase WTe_2 flake (Sec. SII in the Supplemental Material [57]). The crystallographic *a* axis was identified by combining optical microscopy of the flake edges with high-precision polarized Raman spectroscopy (Figs. 2(b) and 2(c); Seec. SIII in the Supplemental Material SIII [57]). As shown in Fig. 2(d), the linear I-V curves confirm high-quality Ohmic contacts. We then measured the nonlinear Hall responses along both the *a* and *b* axes using the lock-in technique (Sec. SIV in the Supplemental Material [57]). Clear signals of the nonlinear Hall effect were observed in both directions [Fig. 2(e)]. Notably, although the *b*-axis response is weaker than the *a* axis, its presence serves as robust evidence for mirror symmetry ($\mathcal{M}_a$) breaking. This establishes the Td-phase WTe_2 as an ideal platform to search for the nonlinear magnetization.

Observation of nonlinear magnetization via SMOKE. Using the same device as in the nonlinear Hall transport measurements, we carried out the optical measurements. Figure 3(a) depicts the polar Kerr setup for detecting out-of-plane magnetization. A linearly polarized laser beam was normally incident and focused onto the sample with applied alternating current (ω=1.177 kHz). The Kerr rotation of the reflected light was collected by a balanced detection system. A lock-in amplifier then demodulated this signal at the first-harmonic frequency (ω=1.177 kHz) to extract MOKE response, and at the second-harmonic frequency (2ω=2.354 kHz) to isolate the SMOKE signal (see Sec. SV in the Supplemental Material [57] for more details). To ensure consistency when switching the current direction between crystallographic axes, the light spot was precisely positioned at the central intersection of the *a* and *b* axes [Fig. 3(b)]. Consequently, by combining a stabilized tunable laser system with real-time intensity monitoring and phase-sensitive lock-in detection, we achieved an ultrahigh Kerr rotation resolution of down to 10 nrad.

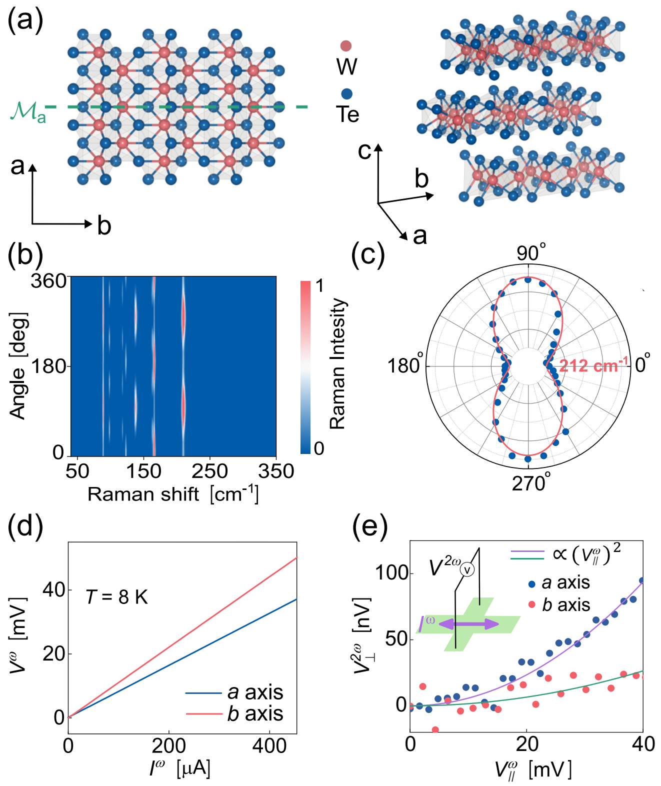

FIG. 2. Crystal structure and electrical transport properties of WTe_2. (a) The crystal structure of WTe_2. The ideal crystal structure of Td-phase WTe_2 only preserves a mirror symmetry $\mathcal{M}_a$ (with the mirror plane indicated by the dashed line). (b) Angle-dependent polarized Raman spectral intensity of a WTe_2 flake used in the device. The measurements were obtained by rotating the laser polarization with respect to the *a* axes. (c) Representative angle-dependent intensities of the Raman peak at 212 cm^{-1}. (d) First-harmonic longitudinal response V^{ω} with the alternating current applied along the *a* and *b* axes. (e) Second-harmonic transverse response $V_{\perp}^{2\omega}$ with the applied alternating current along the *a* and *b* axes (the horizontal coordinate has been converted to the voltage). The dots represent the experimental data, and the solid lines represent the fitted quadratic curves. The inset in (e) shows the measurement setup. Data in (d) and (e) were collected at $T = 8$ K.

As shown in Fig. 3(c) and Fig. S6(a) in the Supplemental Material, MOKE measurements at 8 K show no detectable signal with current applied along either the *a* or *b* axis. In contrast, a pronounced SMOKE signal $\theta_K^{2\omega}$ emerges and exhibits a clear quadratic dependence on the applied current I^{ω} [Fig. 3(d) and Fig. S6(b) in the Supplemental Material], confirming the second-order nonlinear nature of the effect.

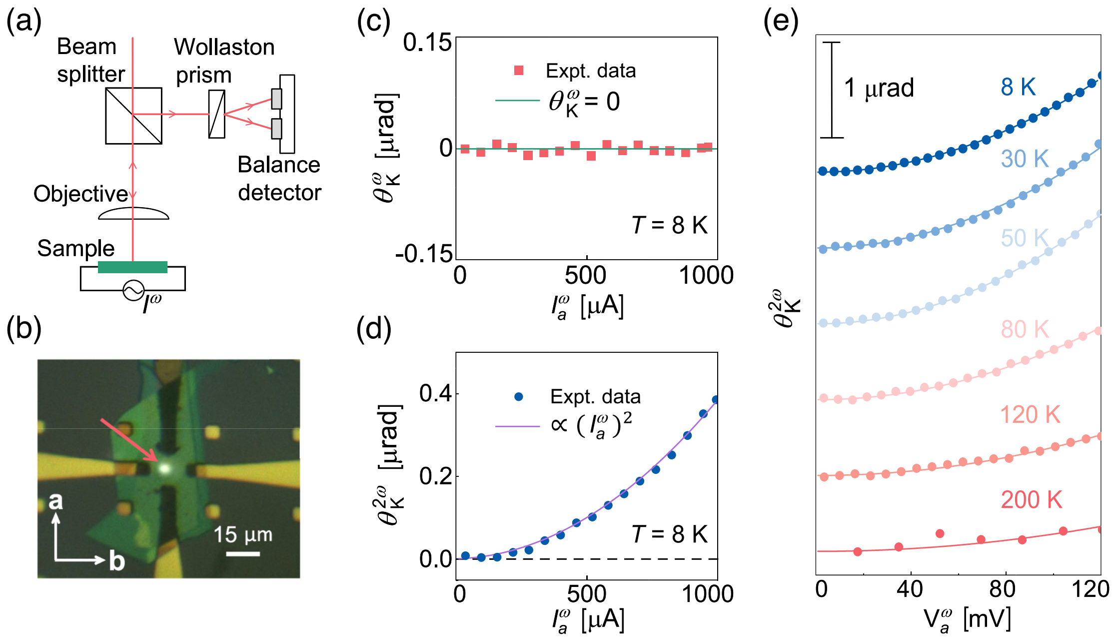

FIG. 3. Observation of SMOKE and temperature dependence. (a) Optical path for polar Kerr measurements. (b) Optical image of the $\mathrm{WTe_2}$ device. The red arrow indicates the light spot. (c) The MOKE signal θ_K^ω as a function of current I_a^ω, and there is no signal within the measurement accuracy. (d) The SMOKE signal $\theta_K^{2\omega}$ as a function of current I_a^ω, the solid line represents a quadratic fit to the data. (e) Temperature dependence of the SMOKE from 8 K to 200 K.

Additionally, to examine the robustness of this effect, we measured the temperature dependence of the SMOKE signal. As shown in Fig. 3(e), $\theta_K^{2\omega}$ maintains a clear and robust presence across a broad temperature range from 8 to 200 K. This observation particularly confirms the high thermal stability of the nonlinear magnetization.

To rule out the alternative origins of the SMOKE signal beyond the nonlinear magnetization, we performed a series of control experiments. First, we confirmed the reproducibility across multiple $\mathrm{WTe_2}$ devices from different batches. All devices exhibited a clear SMOKE signal with no detectable MOKE response, and in most cases, the SMOKE signal persisted up to 200 K (Fig. S7 in the Supplemental Material [57]). Second, to exclude current-induced heating effect, a graphene control device of similar thickness was measured under the same current range, but no SMOKE signal was observed (see Sec. SVI in the Supplemental Material [57]). Particularly, graphene possesses one of the largest third-order nonlinear susceptibilities among all known two-dimensional materials [62], making the absence of a SMOKE signal decisive in ruling out a second-order electro-optic effect origin. Finally, power-dependent SMOKE measurements showed no variation with laser intensity, eliminating laser-induced heating effect (Sec. SVII in the Supplemental Material [57]). Together, these control experiments confirm that the observed SMOKE signal in $\mathrm{WTe_2}$ originates from an electric-field-induced nonlinear magnetization.

Quantum geometric origin of nonlinear magnetization. The nonlinear magnetization induced by a low-frequency (∼kHz) alternating electric field can be generally expressed as

$$\mathbf{M}^{2\omega}(t) = \boldsymbol{\alpha}\mathbf{E}^{\omega}(t)\mathbf{E}^{\omega}(t), \qquad (1)$$

where $\mathbf{M}^{2\omega}(t) = \mathrm{Re}\{\mathbf{M}e^{i2\omega t}\}$ is the magnetization oscillating at frequency 2ω, $\mathbf{E}^{\omega}(t) = \mathrm{Re}\{\mathbf{E}e^{i\omega t}\}$ is the electric field applied at frequency ω, and $\boldsymbol{\alpha} = \boldsymbol{\alpha}^{\mathbf{S}} + \boldsymbol{\alpha}^{\mathbf{O}}$ is the nonlinear magnetization coefficient (a rank-three tensor), with S and O denoting spin and orbital contributions.

By employing Boltzmann kinetics [63] in combination with wavepacket dynamics [15,39], the nonlinear magnetization coefficient α_{ijk} for a time-reversal-symmetric (nonmagnetic) system can be written as (see Sec. SVIII in the Supplemental Material [57] for details)

$$\alpha_{ijk} = \tau e^2 \int [d\mathbf{k}] \Lambda_n^{ijk} f_0', \qquad (2)$$

where (i, j, k) denote the crystallographic directions (a, b, c), τ is the relaxation time of conduction electrons, $-e$ is electron charge, $[d\mathbf{k}]$ represents $\sum_n d^d\mathbf{k}/(2\pi)^d$ with dimension d and band index n, and f_0' denotes the derivative of the Fermi-Dirac distribution with respect to the band energy. The full geometric information of the system is encoded in the quantity Λ_n^{ijk}; it is defined by $\Lambda_n^{ijk} = (F_n^{\mathrm{S},ij} + F_n^{\mathrm{O},ij})v_n^k$, where $\mathbf{F}_n^{\mathrm{S/O}}$ is the spin/orbital polarizability tensor for the nth band [15,64], and $\mathbf{v}_n$ is the intraband velocity. Explicitly, the expressions of $F_n^{\mathrm{S},ij}$ and $F_n^{\mathrm{O},ij}$ are given by

$$F_n^{\mathrm{S},ij} = 2g\mu_B \mathrm{Im} \sum_{m\neq n} \frac{\langle n|s_i|m\rangle\langle m|\partial_j\mathcal{H}|n\rangle}{(\varepsilon_n - \varepsilon_m)^2},$$

$$F_n^{\mathrm{O},ij} = -2\mathrm{Im} \sum_{m\neq n} \frac{m_{nm}^{\mathrm{O},i}\langle m|\partial_j\mathcal{H}|n\rangle}{(\varepsilon_n - \varepsilon_m)^2} - \frac{e}{2\hbar}\epsilon_{ikl}\Gamma_n^{lkj}, \qquad (3)$$

where g is the Landé g-factor for spin, μ_B is the Bohr Magneton, $\hbar$ is the reduced Planck constant, $\mathbf{s} = \boldsymbol{\sigma}/2$ is the dimensionless spin operator, $|n\rangle$ is the Bloch state,

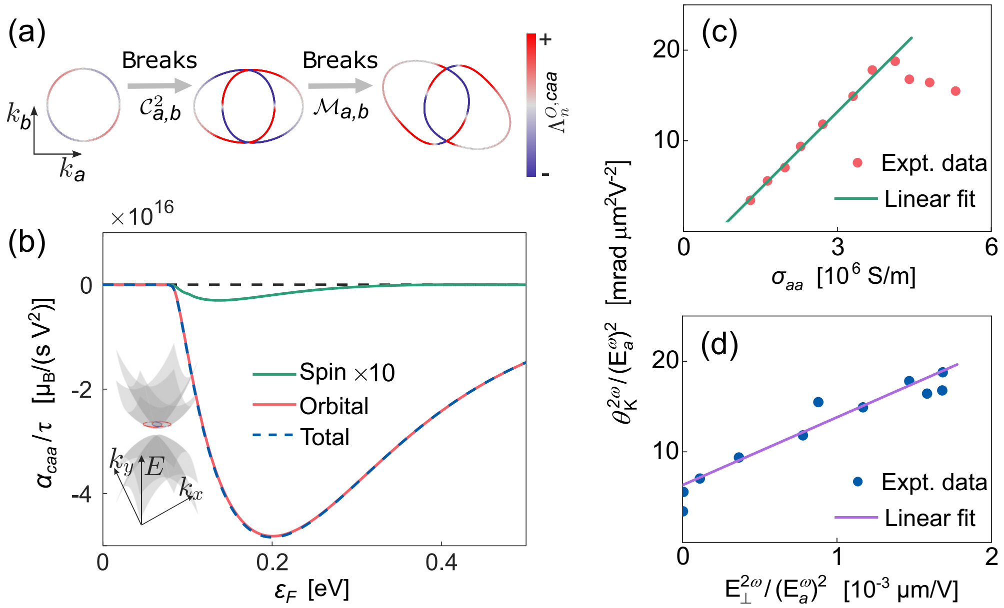

FIG. 4. Theoretical results and scaling analysis. (a) The evolution of Fermi surfaces at Fermi level $\varepsilon_F = 0.25$ eV by breaking twofold rotational symmetries ($\mathcal{C}^2_{a,b}$) and mirror symmetries ($\mathcal{M}_{a,b}$) successively, the colorbar depicts the strength of $\Lambda_n^{\mathrm{O},caa}$. (b) Calculated nonlinear magnetization coefficient α_{caa} as a function of the Fermi energy ε_F. The green, red, and blue represent spin (×10 for visibility), orbital, and total contributions, respectively. The inset depicts the energy dispersion. The model parameters are $v = 1$ eV nm, $t/v = 0.3$, $m = 0.1$ eV, and $b = 1$ eV nm^2 [17]. (c) Scaling behavior between the observed SMOKE signal and linear longitudinal conductivity for different temperatures from $T = 8$ K to $T = 200$ K. (d) Scaling behavior between the observed SMOKE signal and nonlinear Hall signal. The two data points lie on the vertical axis because the nonlinear Hall signal becomes undetectable at $T = 150$ K and 200 K.

$\mathcal{H}$ is the Bolch Hamiltonian, ε_n is the band energy, $\mathbf{m}^{\mathrm{O}}_{mn} = \sum_{l\neq n}(\mathbf{v}_{ml} + \delta_{lm}\mathbf{v}_n) \times \mathcal{A}_{ln}/2$ is the interband orbital magnetic moment, $\mathbf{v}_{mn} = \langle m|\partial_{\mathbf{k}}\mathcal{H}|n\rangle/\hbar$ is the interband velocity, $\mathcal{A}_{mn} = \langle m|\, i\partial_{\mathbf{k}}\, |n\rangle$ is the interband Berry connection, ϵ_{ijk} is the Levi-Civita symbol, and ∂_i is the short of $\partial/(\partial k_i)$. Notably, the second term of $F_n^{\mathrm{O},ij}$ arises from the quantum Christoffel symbol

$$\Gamma_n^{lkj} = \tfrac{1}{2}\left(\partial_j g_n^{kl} + \partial_k g_n^{lj} - \partial_l g_n^{kj}\right), \tag{4}$$

where $g_n^{ij} = \mathrm{Re}\sum_{m\neq n}\mathcal{A}^i_{nm}\mathcal{A}^j_{mn}$ is the quantum metric tensor [1–3]. In Einstein's general relativity, the Christoffel symbol originally characterizes curved spacetime through the geodesic equation [65]. Recently, its quantum version (quantum Christoffel symbol) has been introduced to describe momentum-space gravity [66–68].

Effective model calculations and scaling analysis. To obtain an intuitive understanding of nonlinear magnetization, we establish an effective model that inherits the same symmetry constraints as WTe$_2$. The electronic structure of WTe$_2$ is a type-II semimetal with strong spin-orbit coupling [69–71]. Therefore, the modified Dirac model [17,72] can give the ingredient

$$\mathcal{H} = v(k_a\alpha_a + k_b\alpha_b) + (m - bk^2)\beta + \mathcal{H}', \tag{5}$$

where v, m, b are model parameters, and $\alpha_i = \sigma_a \otimes \sigma_i$, $\beta = \sigma_c \otimes \sigma_0$ are Dirac matrices defined within Pauli matrices $(\sigma_a, \sigma_b, \sigma_c)$. To satisfy the symmetry constraints of WTe$_2$, a symmetry-breaking term $\mathcal{H}' = tk_a\sigma_c \otimes (\sigma_a + \sigma_b + \sigma_c)$ is introduced to break the twofold rotational symmetries $\mathcal{C}^2_{a,b}$ and the mirror symmetries $\mathcal{M}_{a,b}$ but preserve the time-reversal symmetry. Figure 4(a) demonstrates the evolution of Fermi surface by breaking $\mathcal{C}^2_{a,b}$ and $\mathcal{M}_{a,b}$ symmetries successively. Upon symmetry breaking, the Fermi surface exhibits an nonsymmetric distribution of $\Lambda_n^{\mathrm{O},caa}$ in $\mathbf{k}$ space, which coincides the symmetry requirements for a nonzero α_{caa}.

Using Eqs. (2) and (3), we calculate the nonlinear magnetization coefficient α_{caa} for the effective model of WTe$_2$ [Eq. (5)]. Figure 4(b) shows the calculated α_{caa}, including spin, orbital, and total contributions, as a function of the Fermi energy ε_F. Notably, across the entire range of Fermi energy, the orbital contribution remains dominant. To be specific, the orbital contribution is approximately two orders of magnitude larger than the spin contribution. In our experiment, the applied electric field is around 5×10^3 V/m. Then, the induced nonlinear spin magnetization is $5.42 \times 10^{-9}\ \mu_B/\mathrm{nm}^2$, and the orbital magnetization is $1.32 \times 10^{-6}\ \mu_B/\mathrm{nm}^2$ for $\varepsilon_F = 0.2$ eV, $t/v = 0.3$, and $\tau = 1.1$ ps (the estimation of scattering time can be found in Sec. SIX in the Supplemental Material [57]). Therefore, this magnitude of magnetization is sufficient to be detected by our high-precision SMOKE spectroscopy.

Scaling analysis is a powerful tool for distinguishing experimental mechanisms, as demonstrated in studies of the anomalous and nonlinear Hall effects [19,73–75]. This method assumes that, aside from Fermi-surface broadening, the temperature dependence in metals arises predominantly from the relaxation time τ. Since the longitudinal conductivity $\sigma_{aa} \propto \tau$, other response coefficients thus can be expressed as a polynomial in σ_{aa}. Therefore, the specific power-law dependence on σ_{aa} as the temperature varies allows for the determination of the dominant mechanism.

Equation (2) predicts that the quantum geometric nonlinear magnetization is proportional to τ, which implies that the coefficient α_{caa} should scale linearly with the longitudinal conductivity σ_{aa}. This is confirmed by our experimental data in Fig. 4(c) over a broad temperature range. The slight deviation observed below 20 K in Fig. 4(c) is attributed to the proximity of the Fermi level to the band edge in WTe_2 [69–71]. Because the quantum-geometric contribution is strongly concentrated near the band edge [Fig. 4(b)], Fermi-surface broadening becomes non-negligible at these temperatures. This interpretation is further supported by the linear scaling between the SMOKE signal and the nonlinear Hall signal [Fig. 4(d)], as both effects share the same relaxation-time dependence and a similar band-geometry origin [17,18]. Taken together, the scaling analyses in Figs. 4(c) and (d) demonstrate strong mutual consistency between our experiments and theoretical analysis.

Discussion and conclusion. Although the nonlinear Hall effect and the nonlinear magnetization share some similarities, they are fundamentally distinct nonlinear responses. The nonlinear Hall effect is an electric-field-driven charge response governed by the Berry-curvature dipole. In contrast, the nonlinear magnetization is an electric-field-driven magnetic response related to the quantum Christoffel symbol, a geometric quantity. This distinction is also reflected on the experimental side. The nonlinear Hall effect is readily detected via standard transport techniques, while probing nonlinear magnetization requires new measurement capabilities. The SMOKE measurement established here offers a powerful optical route for detecting weak magnetic signals. Additionally, its inherent spatial resolution further provides a foundation for more refined and spatially resolved measurements in future studies.

To summarize, our development of high-sensitivity SMOKE spectroscopy has enabled the direct observation of electric-field-induced nonlinear magnetization in the nonmagnetic semimetal WTe_2. The observed SMOKE signal persists up to 200 K and displays a quadratic dependence on the applied current, highlighting its robust nonlinear nature. Theoretical analysis and scaling law identify the orbital contribution as the dominant mechanism to this nonlinear magnetization. Notably, this orbital contribution is intrinsically related to the quantum Christoffel symbol, thus establishing a direct link between quantum geometry and nonlinear magnetization. Our work offers an experimental paradigm and establishes a fundamental framework for characterizing and understanding nonlinear magnetization. It paves a way toward next-generation orbitronic devices and opens a new avenue for exploring emergent gravity effects in the quantum materials.

Acknowledgments. The authors are indebted to Hao-Jie Lin, Erding Zhao, and Xun Yang for the insightful discussions. This work was supported by the National Key R&D Program of China (2022YFA1405100 and 2022YFA1403700), the National Natural Science Foundation of China (12427805, 12241405, 12350402, 12525401, 12274406, 12174378, 12404146, and 12374077), the CAS Project for Young Scientists in Basic Research (No. YSBR-120), the Guangdong Basic and Applied Basic Research Foundation (2023B0303000011), the Guangdong Provincial Quantum Science Strategic Initiative (GDZX2201001 and GDZX2401001), the Science, Technology and Innovation Commission of Shenzhen Municipality (ZDSYS20190902092905285), the High-level Special Funds (G03050K004), the New Cornerstone Science Foundation through the XPLORER PRIZE, and the Center for Computational Science and Engineering of SUSTech.

Data availability. The data that support the findings of this article are not publicly available upon publication because it is not technically feasible and/or the cost of preparing, depositing, and hosting the data would be prohibitive within the terms of this research project. The data are available from the authors upon reasonable request.

---

[1] J. Provost and G. Vallee, Riemannian structure on manifolds of quantum states, Commun. Math. Phys. **76**, 289 (1980).

[2] J. Anandan and Y. Aharonov, Geometry of quantum evolution, Phys. Rev. Lett. **65**, 1697 (1990).

[3] R. Resta, The insulating state of matter: A geometrical theory, Eur. Phys. J. B **79**, 121 (2011).

[4] P. Törmä, Essay: Where can quantum geometry lead us? Phys. Rev. Lett. **131**, 240001 (2023).

[5] T. Liu, X.-B. Qiang, H.-Z. Lu, and X. C. Xie, Quantum geometry in condensed matter, Natl. Sci. Rev. **12**, nwae334 (2025).

[6] Y. Jiang, T. Holder, and B. Yan, Revealing quantum geometry in nonlinear quantum materials, Rep. Prog. Phys. **88**, 076502 (2025).

[7] S. Peotta and P. Törmä, Superfluidity in topologically nontrivial flat bands, Nat. Commun. **6**, 8944 (2015).

[8] A. Julku, S. Peotta, T. I. Vanhala, D.-H. Kim, and P. Törmä, Geometric origin of superfluidity in the Lieb-lattice flat band, Phys. Rev. Lett. **117**, 045303 (2016).

[9] L. Liang, T. I. Vanhala, S. Peotta, T. Siro, A. Harju, and P. Törmä, Band geometry, Berry curvature, and superfluid weight, Phys. Rev. B **95**, 024515 (2017).

[10] P. Törmä, L. Liang, and S. Peotta, Quantum metric and effective mass of a two-body bound state in a flat band, Phys. Rev. B **98**, 220511 (2018).

[11] K.-E. Huhtinen, J. Herzog-Arbeitman, A. Chew, B. A. Bernevig, and P. Törmä, Revisiting flat band superconductivity: Dependence on minimal quantum metric and band touchings, Phys. Rev. B **106**, 014518 (2022).

[12] S. A. Parameswaran, R. Roy, and S. L. Sondhi, Fractional Chern insulators and the W_∞ algebra, Phys. Rev. B **85**, 241308 (2012).

[13] R. Roy, Band geometry of fractional topological insulators, Phys. Rev. B **90**, 165139 (2014).

[14] T. S. Jackson, G. Möller, and R. Roy, Geometric stability of topological lattice phases, Nat. Commun. **6**, 8629 (2015).

[15] Y. Gao, S. A. Yang, and Q. Niu, Field induced positional shift of Bloch electrons and its dynamical implications, Phys. Rev. Lett. **112**, 166601 (2014).

[16] I. Sodemann and L. Fu, Quantum nonlinear Hall effect induced by Berry curvature dipole in time-reversal invariant materials, Phys. Rev. Lett. **115**, 216806 (2015).

[17] Z. Z. Du, C. M. Wang, H.-Z. Lu, and X. C. Xie, Band signatures for strong nonlinear Hall effect in bilayer WTe_2, Phys. Rev. Lett. **121**, 266601 (2018).

[18] Q. Ma, S.-Y. Xu, H. Shen, D. MacNeill, V. Fatemi, T.-R. Chang, A. M. Mier Valdivia, S. Wu, Z. Du, C.-H. Hsu, *et al.*, Observation of the nonlinear Hall effect under time-reversal-symmetric conditions, Nature (London) **565**, 337 (2019).

[19] Z. Du, C. Wang, S. Li, H.-Z. Lu, and X. Xie, Disorder-induced nonlinear Hall effect with time-reversal symmetry, Nat. Commun. **10**, 3047 (2019).

[20] C. Wang, Y. Gao, and D. Xiao, Intrinsic nonlinear Hall effect in antiferromagnetic tetragonal CuMnAs, Phys. Rev. Lett. **127**, 277201 (2021).

[21] H. Liu, J. Zhao, Y.-X. Huang, W. Wu, X.-L. Sheng, C. Xiao, and S. A. Yang, Intrinsic second-order anomalous Hall effect and its application in compensated antiferromagnets, Phys. Rev. Lett. **127**, 277202 (2021).

[22] A. Gao, Y.-F. Liu, J.-X. Qiu, B. Ghosh, T. V. Trevisan, Y. Onishi, C. Hu, T. Qian, H.-J. Tien, S.-W. Chen, *et al.*, Quantum metric nonlinear Hall effect in a topological antiferromagnetic heterostructure, Science **381**, 181 (2023).

[23] N. Wang, D. Kaplan, Z. Zhang, T. Holder, N. Cao, A. Wang, X. Zhou, F. Zhou, Z. Jiang, C. Zhang, *et al.*, Quantum-metric-induced nonlinear transport in a topological antiferromagnet, Nature (London) **621**, 487 (2023).

[24] X.-B. Qiang, T. Liu, Z.-X. Gao, H.-Z. Lu, and X. C. Xie, A clarification on quantum-metric-induced nonlinear transport, Adv. Sci. e14818 (2025).

[25] V. Edelstein, Spin polarization of conduction electrons induced by electric current in two-dimensional asymmetric electron systems, Solid State Commun. **73**, 233 (1990).

[26] Y. K. Kato, R. C. Myers, A. C. Gossard, and D. D. Awschalom, Current-induced spin polarization in strained semiconductors, Phys. Rev. Lett. **93**, 176601 (2004).

[27] B. A. Bernevig, T. L. Hughes, and S.-C. Zhang, Orbitronics: The intrinsic orbital current in *p*-doped silicon, Phys. Rev. Lett. **95**, 066601 (2005).

[28] T. Tanaka, H. Kontani, M. Naito, T. Naito, D. S. Hirashima, K. Yamada, and J. Inoue, Intrinsic spin Hall effect and orbital Hall effect in 4*d* and 5*d* transition metals, Phys. Rev. B **77**, 165117 (2008).

[29] A. Chernyshov, M. Overby, X. Liu, J. K. Furdyna, Y. Lyanda-Geller, and L. P. Rokhinson, Evidence for reversible control of magnetization in a ferromagnetic material by means of spin–orbit magnetic field, Nat. Phys. **5**, 656 (2009).

[30] D. Fang, H. Kurebayashi, J. Wunderlich, K. Výborný, L. P. Zârbo, R. Campion, A. Casiraghi, B. Gallagher, T. Jungwirth, and A. Ferguson, Spin–orbit-driven ferromagnetic resonance, Nat. Nanotechnol. **6**, 413 (2011).

[31] D. Culcer and R. Winkler, Generation of spin currents and spin densities in systems with reduced symmetry, Phys. Rev. Lett. **99**, 226601 (2007).

[32] J. Železný, H. Gao, K. Výborný, J. Zemen, J. Mašek, A. Manchon, J. Wunderlich, J. Sinova, and T. Jungwirth, Relativistic Néel-order fields induced by electrical current in antiferromagnets, Phys. Rev. Lett. **113**, 157201 (2014).

[33] A. Manchon, J. Železný, I. M. Miron, T. Jungwirth, J. Sinova, A. Thiaville, K. Garello, and P. Gambardella, Current-induced spin-orbit torques in ferromagnetic and antiferromagnetic systems, Rev. Mod. Phys. **91**, 035004 (2019).

[34] D. Go, D. Jo, H.-W. Lee, M. Kläui, and Y. Mokrousov, Orbitronics: Orbital currents in solids, Europhys. Lett. **135**, 37001 (2021).

[35] A. Fert, R. Ramesh, V. Garcia, F. Casanova, and M. Bibes, Electrical control of magnetism by electric field and current-induced torques, Rev. Mod. Phys. **96**, 015005 (2024).

[36] D. Jo, D. Go, G.-M. Choi, and H.-W. Lee, Spintronics meets orbitronics: Emergence of orbital angular momentum in solids, npj Spintron. **2**, 19 (2024).

[37] P. Wang, F. Chen, Y. Yang, S. Hu, Y. Li, W. Wang, D. Zhang, and Y. Jiang, Orbitronics mechanisms, materials and devices, Adv. Electron. Mater. **11**, 2400554 (2024).

[38] X.-B. Qiang, T. Liu, H.-Z. Lu, and X. Xie, Quantum geometric origin of orbital magnetization, Appl. Phys. Lett. **128**, 010501 (2026).

[39] D. Xiao, M.-C. Chang, and Q. Niu, Berry phase effects on electronic properties, Rev. Mod. Phys. **82**, 1959 (2010).

[40] D. Xiao, J. Shi, and Q. Niu, Berry phase correction to electron density of states in solids, Phys. Rev. Lett. **95**, 137204 (2005).

[41] T. Thonhauser, D. Ceresoli, D. Vanderbilt, and R. Resta, Orbital magnetization in periodic insulators, Phys. Rev. Lett. **95**, 137205 (2005).

[42] D. Ceresoli, T. Thonhauser, D. Vanderbilt, and R. Resta, Orbital magnetization in crystalline solids: Multi-band insulators, Chern insulators, and metals, Phys. Rev. B **74**, 024408 (2006).

[43] J. Shi, G. Vignale, D. Xiao, and Q. Niu, Quantum theory of orbital magnetization and its generalization to interacting systems, Phys. Rev. Lett. **99**, 197202 (2007).

[44] T. Yoda, T. Yokoyama, and S. Murakami, Current-induced orbital and spin magnetizations in crystals with helical structure, Sci. Rep. **5**, 12024 (2015).

[45] S. Zhong, J. E. Moore, and I. Souza, Gyrotropic magnetic effect and the magnetic moment on the Fermi surface, Phys. Rev. Lett. **116**, 077201 (2016).

[46] J. Rou, C. Şahin, J. Ma, and D. A. Pesin, Kinetic orbital moments and nonlocal transport in disordered metals with nontrivial band geometry, Phys. Rev. B **96**, 035120 (2017).

[47] J. Son, K.-H. Kim, Y. H. Ahn, H.-W. Lee, and J. Lee, Strain engineering of the Berry curvature dipole and valley magnetization in monolayer MoS_2, Phys. Rev. Lett. **123**, 036806 (2019).

[48] A. L. Sharpe, E. J. Fox, A. W. Barnard, J. Finney, K. Watanabe, T. Taniguchi, M. Kastner, and D. Goldhaber-Gordon, Emergent ferromagnetism near three-quarters filling in twisted bilayer graphene, Science **365**, 605 (2019).

[49] D. Hara, M. S. Bahramy, and S. Murakami, Current-induced orbital magnetization in systems without inversion symmetry, Phys. Rev. B **102**, 184404 (2020).

[50] A. Johansson, Theory of spin and orbital Edelstein effects, J. Phys.: Condens. Matter **36**, 423002 (2024).

[51] D. Allwood, G. Xiong, M. Cooke, and R. Cowburn, Magneto-optical Kerr effect analysis of magnetic nanostructures, J. Phys. D **36**, 2175 (2003).

[52] Y. K. Kato, R. C. Myers, A. C. Gossard, and D. D. Awschalom, Observation of the spin Hall effect in semiconductors, Science **306**, 1910 (2004).

[53] G. Zhang, W. Hübner, G. Lefkidis, Y. Bai, and T. F. George, Paradigm of the time-resolved magneto-optical Kerr effect for femtosecond magnetism, Nat. Phys. **5**, 499 (2009).

[54] C. Stamm, C. Murer, M. Berritta, J. Feng, M. Gabureac, P. M. Oppeneer, and P. Gambardella, Magneto-optical detection of the spin Hall effect in Pt and W thin films, Phys. Rev. Lett. **119**, 087203 (2017).

[55] Y.-G. Choi, D. Jo, K.-H. Ko, D. Go, K.-H. Kim, H. G. Park, C. Kim, B.-C. Min, G.-M. Choi, and H.-W. Lee, Observation of the orbital Hall effect in a light metal Ti, Nature (London) **619**, 52 (2023).

[56] I. Lyalin, S. Alikhah, M. Berritta, P. M. Oppeneer, and R. K. Kawakami, Magneto-optical detection of the orbital Hall effect in chromium, Phys. Rev. Lett. **131**, 156702 (2023).

[57] See Supplemental Material at http://link.aps.org/supplemental/10.1103/dww3-vm74 for (Sec. SI) symmetry analysis of magnetization coefficients, (Sec. SII) device fabrication, (Sec. SIII) polarization-dependent Raman measurement, (Sec. SIV) electrical transport measurements, (Sec. SV) second-harmonic magneto-optical Kerr effect measurements, (Sec. SVI) experimental data in graphene control device, (Sec. SVII) laser intensity dependence of the SMOKE, (Sec. SVIII) theory of nonlinear magnetization, and (Sec. SIX) estimation of scattering time, which includes Refs. [15,20,21,54–56,62,63,76–81].

[58] S. Puri, S. Patel, J. L. Cabellos, L. E. Rosas-Hernandez, K. Reynolds, H. O. H. Churchill, S. Barraza-Lopez, B. S. Mendoza, and H. Nakamura, Substrate interference and strain in the second-harmonic generation from MoSe2 monolayers, Nano Lett. **24**, 13061 (2024).

[59] D. Li, X.-Y. Liu, X.-G. Ye, Z.-C. Pan, W.-Z. Xu, P.-F. Zhu, A.-Q. Wang, K. Watanabe, T. Taniguchi, and Z.-M. Liao, Facilitating field-free perpendicular magnetization switching with a Berry curvature dipole in a Weyl semimetal, Phys. Rev. B **110**, L100409 (2024).

[60] Y. Li, L. Wang, Y. Ouyang, D. Li, Y. Yan, K. Dai, L. Shang, J. Zhang, L. Zhu, Y. Li, and Z. Hu, Extraordinary piezoresponse in free-standing two-dimensional Bi_2O_2Se semiconductor toward high-performance light perception synapse, Mater. Today **83**, 12 (2025).

[61] Z. Zhang, A. Zobelli, C. Gao, Y. Cheng, J. Zhang, J. Caillaux, L. Qiu, S. Li, M. Cattelan, V. Kandyba, A. Barinov, M. Zaghrioui, A. Bendounan, J.-P. Rueff, W. Qi, L. Perfetti, E. Papalazarou, M. Marsi, and Z. Chen, Rotation symmetry mismatch and interlayer hybridization in MoS_2-black phosphorus van der Waals heterostructures, Nat. Commun. **16**, 763 (2025).

[62] Z. Xie, T. Zhao, X. Yu, and J. Wang, Nonlinear optical properties of 2D materials and their applications, Small **20**, 2311621 (2024).

[63] H. Haug and A.-P. Jauho, *Quantum Kinetics in Transport and Optics of Semiconductors* (Springer, 2008), Vol. 2.

[64] H. Wang, Y.-X. Huang, H. Liu, X. Feng, J. Zhu, W. Wu, C. Xiao, and S. A. Yang, Orbital origin of the intrinsic planar Hall effect, Phys. Rev. Lett. **132**, 056301 (2024).

[65] C. W. Misner, K. S. Thorne, and J. A. Wheeler, *Gravitation* (Macmillan, 1973).

[66] T. B. Smith, L. Pullasseri, and A. Srivastava, Momentum-space gravity from the quantum geometry and entropy of Bloch electrons, Phys. Rev. Res. **4**, 013217 (2022).

[67] M. Mehraeen, Quantum response theory and momentum-space gravity, Phys. Rev. Lett. **135**, 156302 (2025).

[68] Y. Onishi, N. Paul, and L. Fu, Emergent curved space and gravitational lensing in quantum materials, Phys. Rev. B **113**, 024401 (2026).

[69] A. A. Soluyanov, D. Gresch, Z. Wang, Q. Wu, M. Troyer, X. Dai, and B. A. Bernevig, Type-II Weyl semimetals, Nature (London) **527**, 495 (2015).

[70] Y. Wang, E. Liu, H. Liu, Y. Pan, L. Zhang, J. Zeng, Y. Fu, M. Wang, K. Xu, Z. Huang, *et al.*, Gate-tunable negative longitudinal magnetoresistance in the predicted type-II Weyl semimetal WTe_2, Nat. Commun. **7**, 13142 (2016).

[71] S.-Y. Xu, Q. Ma, H. Shen, V. Fatemi, S. Wu, T.-R. Chang, G. Chang, A. M. M. Valdivia, C.-K. Chan, Q. D. Gibson, *et al.*, Electrically switchable Berry curvature dipole in the monolayer topological insulator WTe_2, Nat. Phys. **14**, 900 (2018).

[72] X.-B. Qiang, Z. Z. Du, H.-Z. Lu, and X. C. Xie, Topological and disorder corrections to the transverse Wiedemann-Franz law and Mott relation in kagome magnets and Dirac materials, Phys. Rev. B **107**, L161302 (2023).

[73] N. Nagaosa, J. Sinova, S. Onoda, A. H. MacDonald, and N. P. Ong, Anomalous Hall effect, Rev. Mod. Phys. **82**, 1539 (2010).

[74] Z.-H. Gong, Z. Z. Du, H.-P. Sun, H.-Z. Lu, and X. C. Xie, Nonlinear transport theory at the order of quantum metric, arXiv:2410.04995.

[75] Z.-H. Gong, Z.-H. Wei, H.-Z. Lu, and X. C. Xie, Identifying geometric third-order nonlinear transport in disordered materials, arXiv:2510.24239.

[76] I. H. Kao, R. Muzzio, H. Zhang, M. Zhu, J. Gobbo, S. Yuan, D. Weber, R. Rao, J. Li, J. H. Edgar, *et al.*, Deterministic switching of a perpendicularly polarized magnet using unconventional spin-orbit torques in WTe_2, Nat. Mater. **21**, 1029 (2022).

[77] I. Lyalin and R. K. Kawakami, Interface transparency to orbital current, Phys. Rev. B **110**, 104418 (2024).

[78] P. He, G. Koon, H. Isobe, J. Tan, J. Hu, A. Neto, L. Fu, and H. Yang, Graphene moiré superlattices with giant quantum nonlinearity of chiral Bloch electrons, Nat. Nanotechnol. **17**, 378 (2022).

[79] Hurd, *The Hall Effect in Metals and Alloys* (Plenum Press, 1972).

[80] Ashcroft and Mermin, *Solid State Physics* (Thomson Learning, 1976).

[81] C. Xiao, W. Wu, H. Wang, Y.-X. Huang, X. Feng, H. Liu, G.-Y. Guo, Q. Niu, and S. A. Yang, Time-reversal-even nonlinear current induced spin polarization, Phys. Rev. Lett. **130**, 166302 (2023).